THE SEISMIC PERFORMANCE OF STEEL ENCASED REINFORCED CONCRETE BRIDGE PILES

R.J.T. Park*, M.J.N. Priestley**, and W.R. Walpole***

SYNOPSIS:

An experimental and theoretical investigation into the seismic performance of steel encased reinforced concrete bridge piles is described. Six test units were designed, constructed and tested under cyclic lateral displacement-controlled loading. The units had an outside diameter of 360 mm and a steel casing thickness of 5 mm. Variables included the axial load level, inclusion or exclusion of internal reinforcing cages, and the influence of the casing continuity at he critical flexural sections. Sound seismic performance was observed in all of the models and good agreement between predicted and observed ultimate behaviour was obtained.

GLOSSARY OF TERMS:

A_g = gross area

A_{sp} = section area of spiral reinforcement

D = outside diameter of casing

D_s = diameter across spiral reinforcement

E_s = Young's modulus for steel

f_h = hoop stress in the casing

f_ℓ = longitudinal stress in the casing

$f_{\ell h}$ = shear stress in the casing

f_s = steel "

f_u = ultimate steel stress

f_y = yield stress

f'_c = concrete cylinder strength

H = lateral force

H_{ACI} = lateral force at ACI flexural capacity

I = second moment of area

M = moment at stub face

P = axial load

Q = first moment of area of the casing above a diameter

s = pitch of spiral reinforcement

t = casing thickness

V_{spiral} = shear force carried by spiral reinforcement

x_i = distance from the pin connection to the ith strip

$\gamma_{h\ell}$ = shear strain in the casing

Δ = lateral displacement of stub

Δ_x = length of strip

Δ_y = yield displacement

ε_c = concrete strain

ε_h = hoop strain

ε_ℓ = longitudinal strain

ε_{spiral} = spiral reinforcement strain

μ = displacement ductility factor

μ_T = " " " - top position

μ_B = displacement ductility factor - bottom position

ν_s = Poisson's ratio for steel

$\Sigma|\mu|$ = cumulative displacement ductility factor

ρ_s = volumetric confinement ratio

τ = shear stress

ϕ_i = curvature in the ith strip

ϕ_{peak} = angle from the principal strains to the hoop or longitudinal direction

ϕ_y = yield curvature

INTRODUCTION:

It has not been common practice to design bridge pile systems for ductility under seismic attack. However, the vagaries of soil-pile interaction, certain potential for fluctuations in river bed level, and the dynamic response of structural systems common in bridging, imply that plastic hinging of piles may be impossible to prevent. Doubts have also existed with regard to the effects of corrosion on the casing and the efficiency of composite action in the section, with the result that it has become standard New Zealand Railways' practice to neglect

*Graduate student, University of Canterbury, Christchurch, New Zealand and Assistant Engineer, New Zealand Railways
**Reader in Civil Engineering, University of Canterbury, Christchurch, New Zealand
***Senior Lecturer in Civil Engineering, University of Canterbury, Christchurch, New Zealand

the presence of the casing. Because of the common usage of steel encased reinforced concrete piles for bridges in New Zealand, it was felt that their performance under axial and cyclic flexural loading, simulating seismic attack, should be investigated.

Relevant research already performed includes tests on steel tubes, infilled with concrete (1,2) under monotonically increasing axial load, which showed ductile performance. Extensive testing has also been performed on reinforced and prestressed concrete (e.g. 3,4) members under simulated seismic attack; which suggested that sound performance was dependent on provision of adequate spiral reinforcement.

The theoretical structural response of cased piles is complicated by the state of biaxial stress in the casing; which is subjected to shear stresses, longitudinal stresses from the axial load and flexure in the pile, and hoop stresses due to its concrete confinement role. The interaction of these stresses under post-elastic cyclic conditions is extremely complicated. An additional complication is the potential for local instability in the casing resulting in a buckling on the compression side.

In an attempt to quantify these effects, six model piles were tested under simulated seismic loading and the experimental results compared with theoretical predictions based on monotonic loading moment-curvature analyses.

DESCRIPTION OF TEST UNITS:

The six circular test units constructed all had the same basic dimensions of 360 mm outside diameter D, 3.9 m total height, and 5 mm casing wall thickness t. They were essentially tested as vertical beams with a central lateral load. One of the test units in the loading frame is illustrated in Figure 1. Axial load was provided by a 10 MN DARTEC electro-hydraulic Universal Testing Machine, and lateral load by a 500 kN MTS jack. No attempt was made to realistically model soil-pile interaction beyond the approach of assuming that the pile was fixed at some depth in the ground. Figure 2 illustrates the loads and bending moments on the models and the prototypes. Although the moment pattern of the model does not duplicate that of the prototype it can be considered that the two cantilevers, above and beneath the central stub, represent the part of a pile between the point of maximum moment and the contra-flexure point. The central stubs were heavily reinforced to ensure that critical sections occurred in the piles at the faces of the stub and not within the stub. Figure 3 illustrates a typical prototype pile section and the approximately 4/9th scale section that was adopted for the test series.

The test units were arranged in three pairs with one of each pair of units tested at an axial load ratio, P/f'_cAg, of 0.1 and the other at 0.3. The first pair of units, 1 and 2, consisted of continuous concrete-filled tubes without additional reinforcement. Units 3 and 4 consisted of continuous concrete-filled tubes reinforced with longitudinal and spiral reinforcement as shown in Figure 3. Units 5 and 6, simulating typical New Zealand Railways bridge abutment piles, were also reinforced as shown in Figure 3 and were constructed with the casing embedded only 50 mm into the central stub, leaving a gap of 300 mm in the continuity of the casing at midheight of the units. The spiral reinforcement spacing, casing steel and main bar embedment are illustrated in Figure 4.

The spiral reinforcement was designed to the requirements of the New Zealand Concrete Code, NZS 3101 (5), neglecting, as is normal practice, the influence of the casing. Shear criteria were found to govern, resulting in a tighter spiral reinforcement pitch for the test units under $P/f'_cAg = 0.1$. However, inadvertently, the models were tested in inverted order implying that units with greater axial load contained excess spiral reinforcement; whilst the units with lower axial load contained inadequate spiral reinforcement. It was felt that this was not a serious error as the volumetric confining ratios ρ_s were 5.8%, 2.9%, and 1.4%; for the casing, the R10-35 (10 mm diameter non-deformed bars at 35 mm centres), and the R10-70 centres respectively. Thus it was expected that the effect of the casing, though ignored in design, would dominate behaviour.

It was also of some relevance to note Clause 6.3.12.6(a) of NZS 3101 (5) which provides an equation for the design of steel encasements in composite columns and piers.

$$t \geq D\sqrt{\frac{f_y}{8\,E_s}} \qquad (1)$$

where f_y = steel yield stress, and
E_s = steel Young's modulus.

This criteria is based on the attainment of longitudinal yield strength in the casing prior to the commencement of local buckling. However, the nature of the analyses or tests to verify this equation are not stated, although it is probably that they are based on tests of steel tubes with monotonically applied axial loads. Equation (1) gave a value of encasement thickness $t = 5.4$ mm based on actual material properties compared to the value of 5 mm which was used in the experimental series.

MATERIAL PROPERTIES:

Concrete was supplied by a ready-mix contractor. The concrete inside the casing had a maximum aggregate size of 13 mm and a slump of 150 mm. Compression strengths of 28 MPa and 29 MPa were obtained for units 1 to 4 and units 5 to 6 respectively at time of testing the units.

Typical stress-strain curves for the longitudinal D16 (16 mm diameter, deformed bar, grade 275 MPa yield) bars, the R10 spiral reinforcement, and the steel

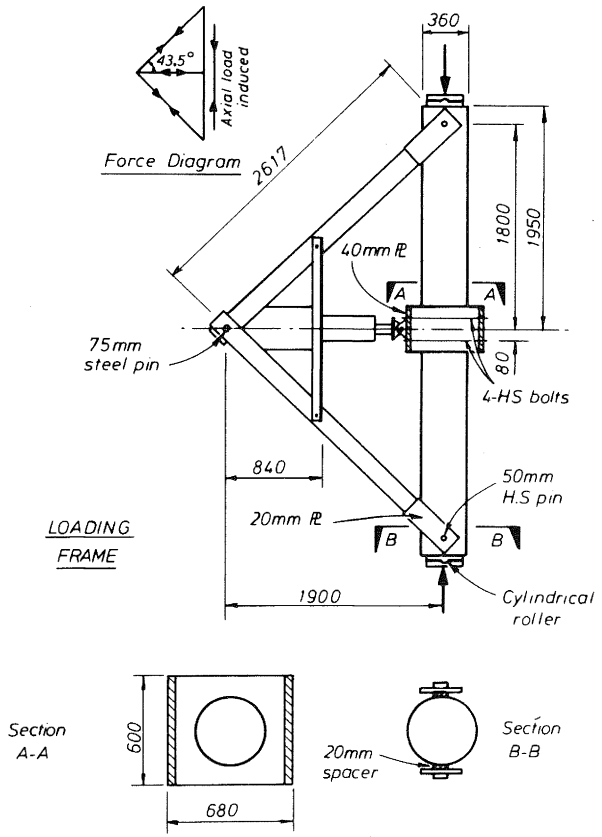

Fig. 1 - A Test Unit in the Loading Frame

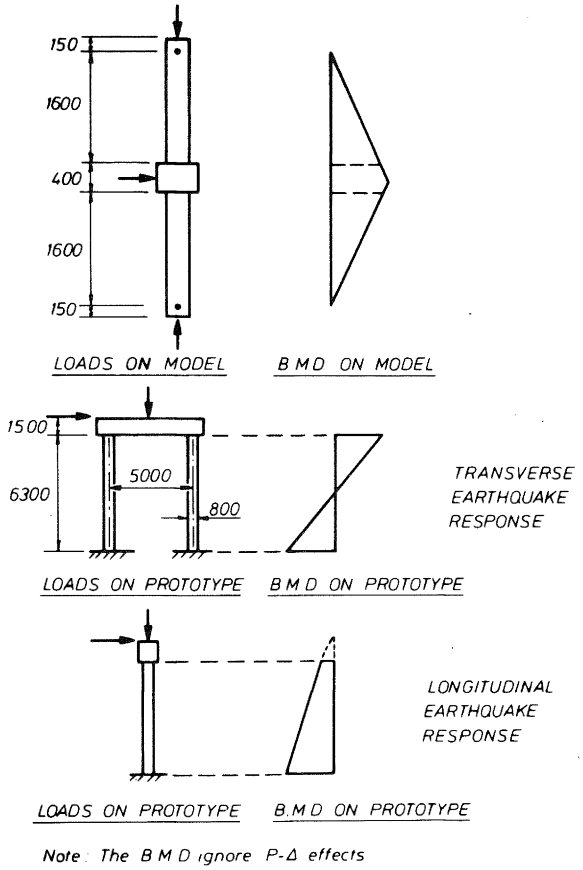

Fig. 2 - Comparison of Bending Moment Diagrams

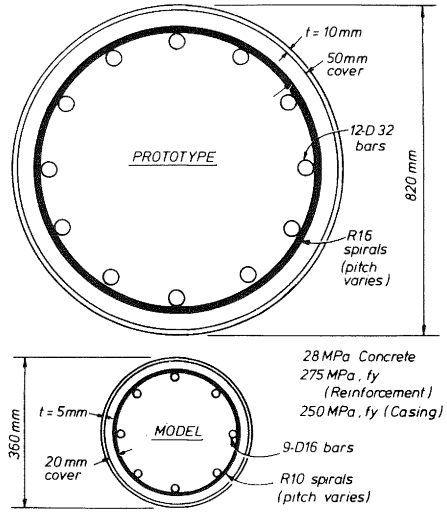

Fig. 3 - Model and Prototype Sections with Design Strengths

encasement are shown in Figure 5. Of particular interest are the characteristics of the casing steel. Samples cut from flat plate and the longitudinal direction of rolled casing gave a yield stress of 370 MPa with strain hardening commencing by 1% strain indicating behaviour more characteristic of grade 380 steel than the specified mild steel. The samples cut from the hoop direction of the rolled casing and then restraightened for testing showed the elimination of a yield point as well as resulting in higher stresses at comparatively low values of strain. This was associated with the cold working of the steel as it was bent to the required radius and subsequently restraightened for testing. The maximum strain resulting from cold working was 1.4%. It is probable that the actual characteristics of the casing steel in the hoop direction were intermediate between the flat plate and hoop element samples.

A summary of the actual test unit details is provided in table 1.

INSTRUMENTATION:

Longitudinal strains and curvatures in the vicinity of the plastic hinge zones on either side of the central stub were measured by linear potentiometers and dial gauges, mounted on stands tack welded to the casing. Lateral deflection and twist of the control stub were also measured using linear potentiometers. A large number of electrical resistance strain gauges were fixed to the casing, spiral reinforcement, and longitudinal bars to enable strains within the plastic hinge zones to be monitored. Full details of instrumentation are given in reference 6.

LOAD SEQUENCES:

An initial cycle of static loading to 75% of the theoretical ultimate lateral load, H_{ACI}, was applied in both the forward (North) and reverse (South) directions. From the resulting load-deflection plot an experimental value for the yield displacement, Δ_y, was obtained by extrapolating a straight line from the origin through the peak load-deflection point obtained, to the theoretical ultimate load. For this purpose H_{ACI} was based on strain compatibility using the measured steel yield strengths, f_y, the concrete unconfined compression strength, f'_c, an ultimate concrete strain of 0.003 and the A.C.I. stress block for concrete in compression. The casing steel was ignored in strength computations for units 5 and 6. The value of Δ_y obtained this way is greater than that which would have been obtained at first yield of the steel, and corresponds to an elasto-plastic approximation of load-displacement behaviour.

After this initial cycle, static cyclic loading to increasing displacement levels was applied to the models. All units were subjected to a minimum of 2 cycles at each of displacement ductility levels, μ, of $\pm$ 2, 4 and 6. Finally, dynamic testing at a frequency of 0.13 Hertz and amplitude of approximately $\pm$ 65 mm was carried out.

THEORETICAL BEHAVIOUR:

In a simple attempt to theoretically model behaviour, monotonic moment-curvature analyses were carried out, assuming the casing to behave in accordance with a number of different hypotheses. The interaction of the flexural, shear and confinement roles of the casing is a complication which distinguishes the steel-cased member from conventionally reinforced concrete which has relatively little interaction between these three actions. A simplistic analysis based on the von Mises yield criterion - equation (1), the maximum likely level of shear stress in the casing $f_{\ell h}$, and the actual yield stress f_y, in the casing showed that the reduction in longitudinal stress f_ℓ and hoop stress f_h due to shear was negligible.

viz: $$f_y^2 = f_\ell^2 + f_h^2 - f_\ell . f_h + 3f_{\ell h}^2 \quad (2)$$

$f_y = 370$ MPa

$f_{\ell h} \leq 50$MPa based on the maximum shear force expected during testing - which was assumed to be carried solely by the casing.

Hence $$\left(\frac{3f_{\ell h}^2}{f_y^2}\right)_{max} = 5\%$$

Thus the 5% of the section's capacity taken by shear was unlikely to significantly influence the interaction between f_ℓ and f_h. The analysis was considered simplistic because the von Mises yield criterion is not designed for post-elastic deformations.

It is also well known that peak circumferential stresses resulting from confinement and shear are separated by 90°, indicating again that interaction between these two effects should not be significant. Consequently interaction between flexural and confinement roles of the casing was the prime concern.

Units 1-4 (Continuous Casing)

Upper Bound Approach: For units 1 to 4 it was evident that an "upper bound" approach would assume full composite action with the uniaxial stress-strain relationship of the casing applying in both the hoop and longitudinal directions. Hence the casing could be assumed to develop its full strength in flexure; and the concrete could be assumed to follow a confined stress-strain relationship, as shown later, with the casing fully contributing to concrete confinement.

Lower Bound Approach: The unknown bond conditions at the interface of the concrete and the casing, and the variation in

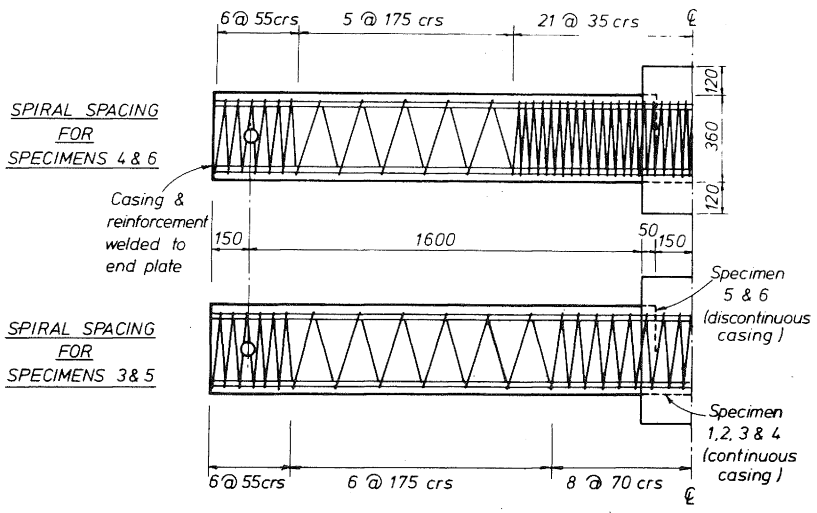

Fig. 4 - Spiral Reinforcement Spacing, and Casing Steel and Main Bar Embedment

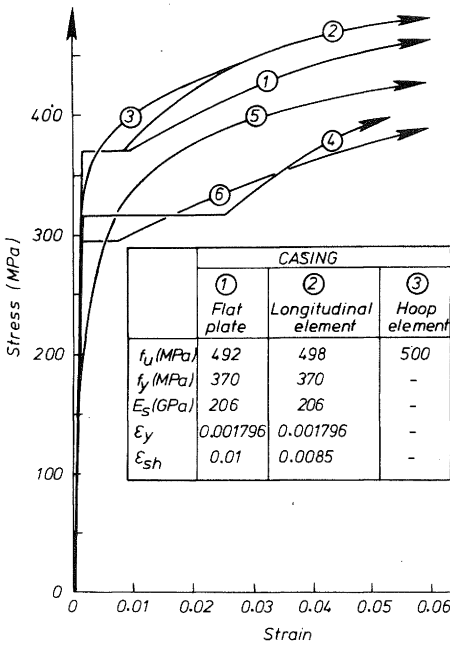

	CASING			D16	R10	
	① Flat plate	② Longitudinal element	③ Hoop element	④	⑤ Restraightened	⑥ Straight
f_u (MPa)	492	498	500	463	449	413
f_y (MPa)	370	370	-	315	-	295
E_s (GPa)	206	206	-	206	-	206
ε_y	0.001796	0.001796	-	0.001529	-	0.001432
ε_{sh}	0.01	0.0085	-	0.025	-	0.007

Fig. 5 - Tensile Stress-Strain Curves for the Casing Steel, D16 Reinforcement, and R10 Reinforcement

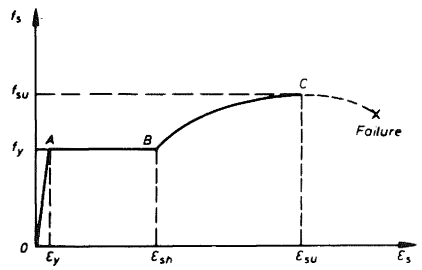

Fig. 6a - Analytical Stress-Strain Curve for Uniaxially Loaded Steel

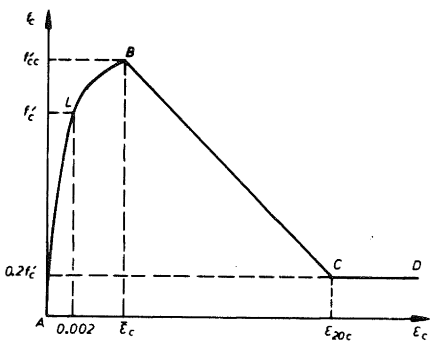

Fig. 6b - Analytical Stress-Strain Curve for Confined Concrete

concrete dilatancy around the section, implied that the hoop tension distribution around the casing was difficult to assess. A possible "lower bound" approach still assuming full composite action, resulted from the assumption that the casing had its uniaxial stress-strain characteristics in the longitudinal direction, but that it had no confining effect on the concrete. In this case the concrete stress-strain relationship depended on its uniaxial behaviour modified, for units 3 and 4 by confinement provided by spiral reinforcement.

Other Approaches: The theoretical response of the steel tube alone, and the reinforced concrete alone, were also examined, as was the effect of the reinforced concrete section confined by the tube with no contribution of the tube to flexure. These last three alternatives produced strengths lower than the fully compatible "lower bound" approach described above, and represented different possible models for behaviour where composite action did not occur.

Units 5 and 6 (Discontinuous Casing)

For units 5 and 6 which did not have continuous casing throughout their length, predicted strength was based on properties of the reinforced concrete section, with the casing contributing only to concrete confinement. This was because at the face of the stub, which was assumed to be the critical section, there was only 50 mm anchorage of the casing. Consequently bond failure between casing and concrete was expected to reduce the casing moment capacity at the critical section to insignificant levels. However, the elastic stiffness of units 5 and 6 was expected to be only slightly smaller than that of units 3 and 4 since sections away from the loading block should display reasonable bond between the casing and the concrete.

Concrete and steel Stress-Strain Models

Full details of the stress-strain models are provided elsewhere (6). The concrete stress-strain curve adopted was that developed by Leslie (7) for circularly confined concrete. This curve takes into account the increase in strength and ductility of the concrete, due to the confinement provided by spiral reinforcement and the steel tube. The concrete curve was that developed by Mander (8). The model took into account the normal elastic-plastic assumption of steel behaviour and also modelled the strain-hardening range. The commonly made assumption of steel behaviour being identical in tension and compression was also followed. The two stress-strain curves are illustrated in Figure 6.

Theoretical Moment-Curvature Results

Theoretical moment-curvature curves based on the various hypotheses described previously are plotted for the six units in Figure 7.

Considering the curves which illustrated the upper and lower bound responses for units 1 to 4, it is evident that very nearly identical responses are predicted well into the inelastic range. It is also worth noting that units 3 and 4 which had internal spiral reinforcing, gave very close upper and lower bound responses compared with units 1 and 2 which did not have internal spiral reinforcement. The difference in predicted strength between units 5 and 6, which did not possess continuous casing at the critical section, and the other units is also clearly contrasted, as is the potential loss of strength if composite action did not occur and the steel tube carried the load alone. The weakest possible response of the models is indicated by the response of the concrete core section assumed to be confined by spiral reinforcement where the concrete outside the spiral reinforcement was assumed to all spall at an extreme concrete compression fibre strain of 0.004.

Theoretical monotonic load-deflection responses were also computed to compare with the experimental cyclic results. These were obtained as follows. Given the bending moment distribution a curvature diagram can be deduced from the theoretical moment-curvature relationship. The deflection for the given moment distribution is given by the first moment of area of the curvature diagram about the hinged connection with the reaction frame as shown in equation (3) and Figure 8.

$$\Delta = \Sigma\ \phi_i . x . \Delta_x \qquad (3)$$

where Δ = lateral deflection at unit mid-height, ϕ_i = average curvature in the ith strip, x_i = distance of the ith strip from the hinged connection, Δ_x = increment of length.

Moment equilibrium at the face of the central stub implies

$$H = 1.25\ (M - 1.094P.\Delta) \qquad (4)$$

where H = lateral jack force, M = moment at the face of the central stub, and P = axial load.

Thus equations (3) and (4) allowed the computation of the theoretical monotonic load-deflection response allowing for the P-Δ effect. Figure 8 also shows the theoretical curvature distributions in the test units. Units 1 to 4 which had continuous casing were assumed to have the same pile curvature inside the stub as at the face of the stub as the bond between the casing and the stub concrete was likely to be poor. Units 5 and 6 were anticipated to have low curvature inside the stub, due to the stub's rigidity when compared with that of the pile.

EXPERIMENTAL RESULTS:

General Behaviour of the Test Units

Performance of units 1 to 4 with continuous casings, was strongly influenced by the development of local buckling at the critical sections, which extended over an axial length of about 60 mm as

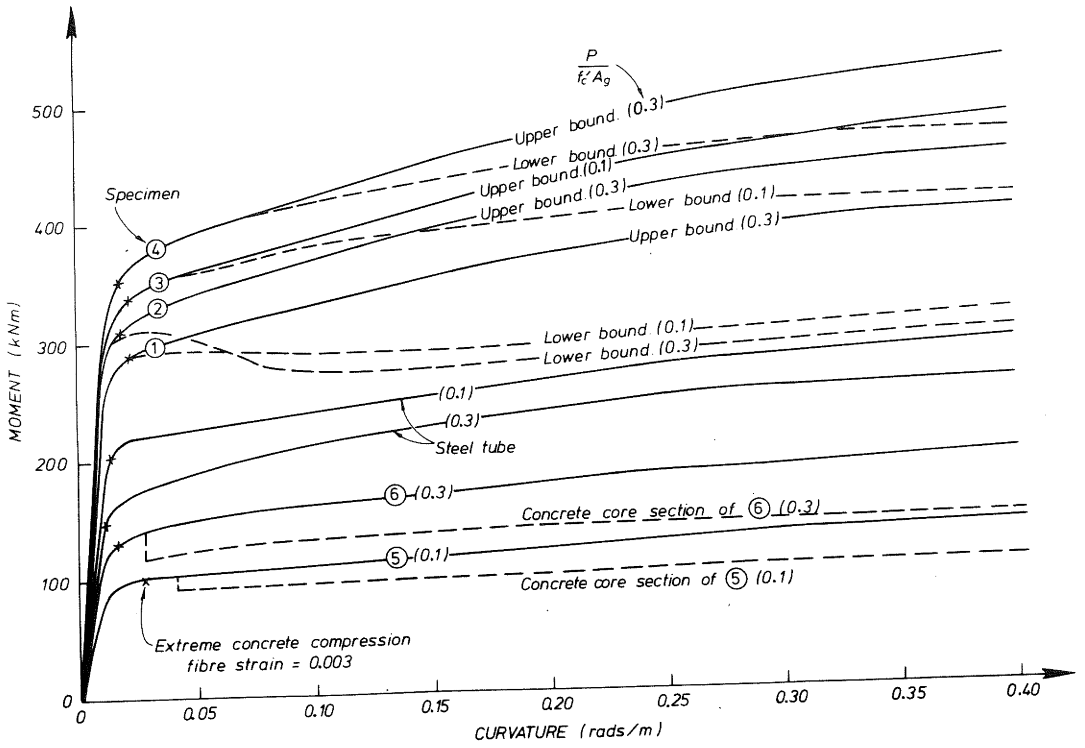

Fig. 7 - Theoretical Moment-Curvature Responses

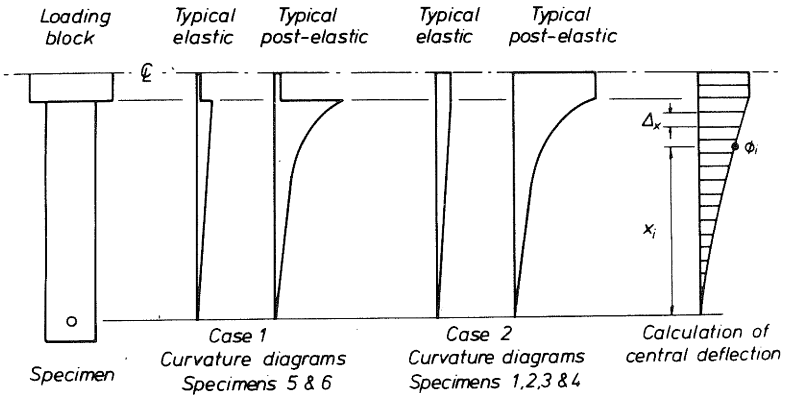

Fig. 8 - Curvature Diagrams

shown in Figure 9a, and formed on the first cycle to a ductility level of $\mu = \pm 4$ for each of the four units. The bulging initially formed at only the extreme compression fibres of the section and grew to a maximum outstand of approximately 15 mm by the end of static testing. However, the local buckling only appeared to influence the strength of unit 1 which was subjected to an axial load of $0.1 f'_c A_g$ and had no internal reinforcement. This unit suffered strength degradation when the buckling spread right around the perimeter of the critical sections. Under dynamic loading, horizontal fracturing of the units at the bulging positions occurred for units 1 and 2 which had no internal spiral reinforcement. Removal of the casing at the North and South faces adjacent to the block, after completion of testing, revealed that the concrete just beneath the bulging regions was crushed, as shown in Figure 9b, whilst concrete outside the bulging region was not crushed. It is inferred from this that the 60 mm axial length of buckled casing represents the zone of concentrated plastic damage. It was also visually obvious during testing that the rotation was concentrating on the buckled regions.

Units 5 and 6, with discontinuous casings, performed very well. Unit 6, with R10 spiral reinforcement at 35 mm centres in the critical plastic regions, appeared practically indestructible; and unit 5, with R10 spiral reinforcement at 70 mm centres in the critical plastic regions was still performing very well after extensive static cycling to a cumulative displacement ductility level, $\Sigma|\mu|$, of 291. Slipping of the casing relative to the concrete loading block was evident during testing, and in the case of unit 5 there was visual evidence, as shown in Figure 9c, of the internal concrete sliding relative to the casing on the side subjected to longitudinal tension. Thus it was clear that the casing and the internal reinforced concrete core were not acting compositely, and that the critical section was at the curtailment of the casing 50 mm inside the central stub.

Load-Deflection Response

The lateral load-lateral deflection response of units 1, 3 and 6 during the static phase of testing are illustrated in Figures 10a, 10b and 10c respectively. The fully composite upper and lower bound theoretical monotonic loading predictions, and the theoretical ultimate strength, H_{ACI} based on actual yield strength and an ultimate concrete strain of 0.003, at the yield deflection, Δ_y, are also included in this figure, as is the effect of secondary moments due to axial load - the so-called P-Δ effect. It should be noted that the P-Δ effect has also been included in the upper and lower bound theoretical load-deflection curves.

The behaviour of units 1 to 4 were all similar, although unit 1 displayed greater strength degradation due to local buckling of the casing than did the other units. From Figures 10a and 10b it can be seen that the upper bound prediction is a good envelope to behaviour up to $\mu = \pm 4$, when buckling was initiated, whilst above this level the envelope of the cyclic response tended to lie between the upper and lower bound prediction. It is also obvious from the theoretical response of the steel tube alone, that this provided the major part of the flexural strength from composite action of casing and core.

The envelope of the cyclic response also indicates that strength appreciably in excess of the theoretical strength, H_{ACI} taking into account P-Δ effects, is available to high displacement levels. Hysteresis loops for units 1 to 4 exhibited little loss of strength and stiffness at the peaks of each cycle, apart from the last cycle for unit 1. However, through the middle range of deflections there was significant degradation in stiffness, especially at the cycles to $\mu = \pm 6$. This can be attributed to the low axial stiffness in tension of the casing as the region previously buckled in compression was restraightened, and to the low concrete stiffness as cracks in a previously tension region were closed under load reversal. Wide cracking in the central stub was apparent at the later stages of testing and this was thought to be responsible for the degradation of performance of unit 3 at high ductility levels.

Figure 10c shows the response of unit 6; behaviour of unit 5 was very similar. The hysteresis loops exhibited little strength and stiffness degradation at the peaks of each cycle; and strength well in excess of both the equivalent A.C.I. capacity, H_{ACI}, and the theoretical response was achieved. The strength increase from that theoretically predicted, was probably due to two causes. (1) - The compressive stresses developed in end bearing of the casing as it pushed into the heavily confined central stub. (2) - Test units 5 and 6 were much stiffer than was predicted by ignoring the stiffness of the casing and thus strength would be gained at a lower deflection level than theoretically predicted. The loops were significantly pinched in the middle range of deflections probably due to: shear deformation, wide opening of concrete cracks and the lack of end bearing for the steel casing at that stage. In the case of unit 6 very little damage was inflicted during dynamic testing consisting of 81 cycles at $\mu = \pm 20$, so a further phase of static testing was carried out which showed the model still had strength in excess of the theoretical prediction even at ductility levels as high as $\mu = 40$. Unit 6 also appeared to be stronger in one direction than the other; this was due to a sag created in the unit during construction.

Strains in the Casing

Strain rosettes were located around sections 100 mm from the central block. Since buckling for units 1 to 4 occurred over the 60 mm region immediately adjacent

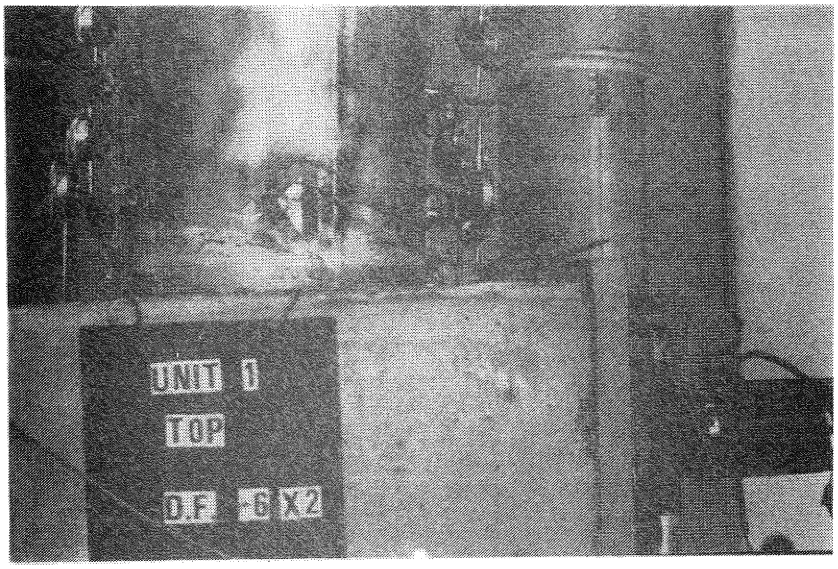

Fig. 9a - Local Buckling

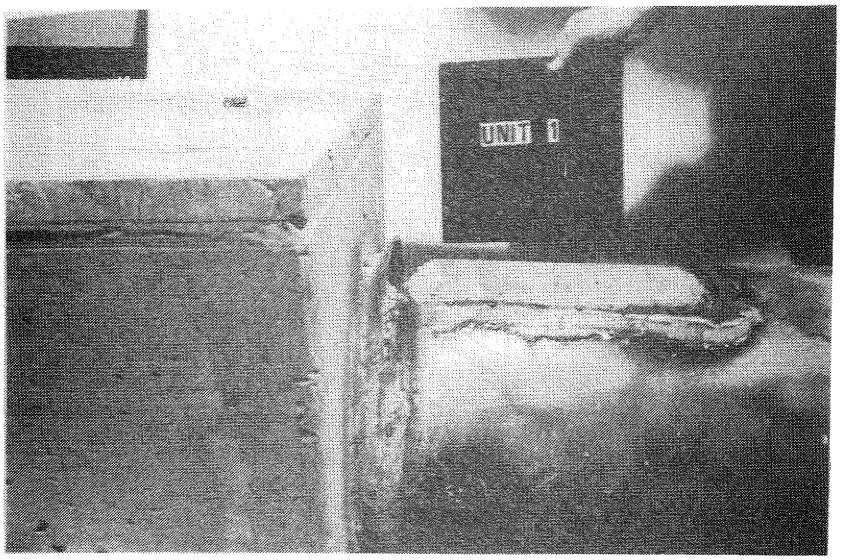

Fig. 9b - Crushed Concrete

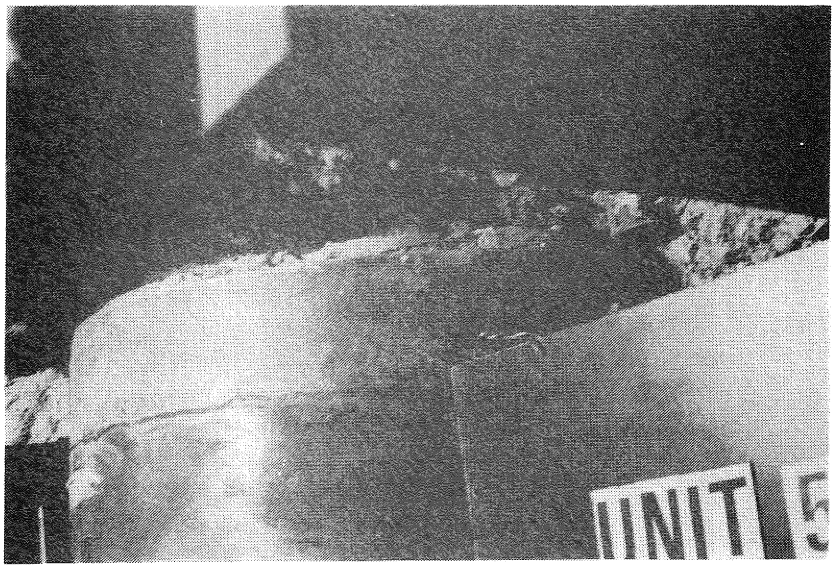

Fig. 9c - Slipping of the Core Concrete Through the Casing

(a)

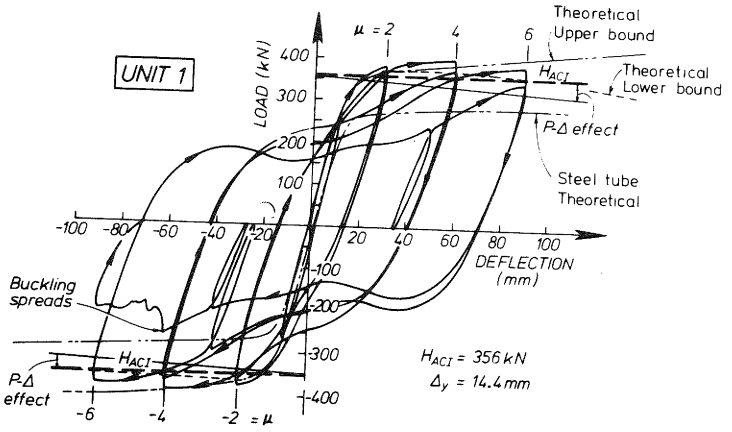

(b)

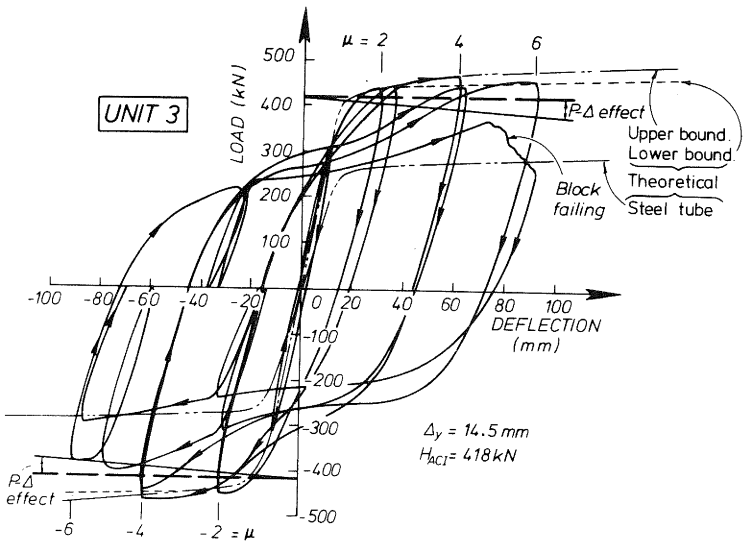

(c)

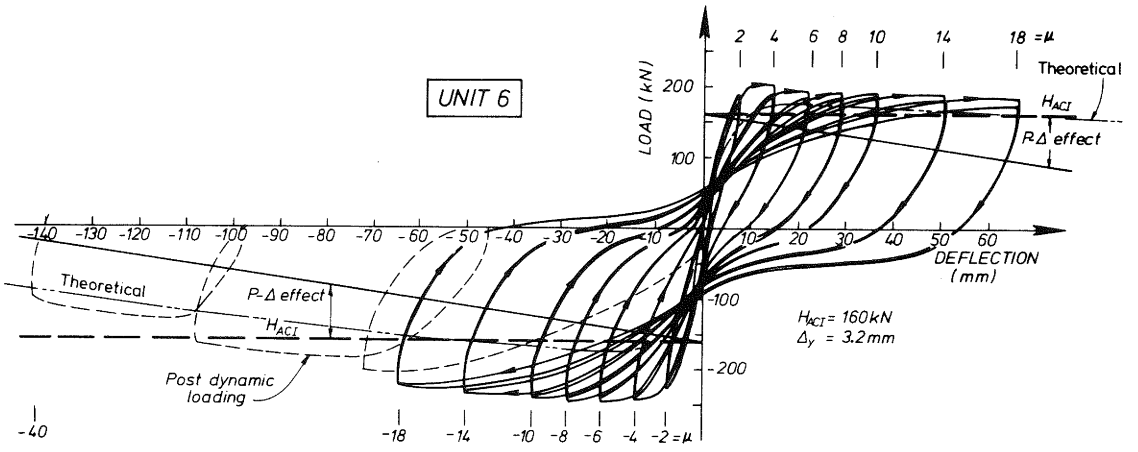

Fig. 10 - Static Loading Lateral Load-Lateral Deflection Responses

to the block, it is probable that the strains recorded were lower than the maximum strains in the casing.

The variation of shear strain $\gamma_{h\ell}$, and the angle ϕ_{peak} from the direction of principal strains to the hoop or longitudinal direction with the magnitude of the displacement ductility factor just above $|\mu_T|$ and beneath $|\mu_B|$ the block for sections of unit 3 is illustrated in Figure 11. These results which were typical of those for units 1 to 4 show a good deal of scatter. However, it is evident that the rosettes away from the loading axis generally indicate higher values of $\gamma_{h\ell}$ and ϕ_{peak} than those along the loading axis. The uniaxial loading yield strain was exceeded by a displacement ductility level of 5.

The variation of confining strain, which may be expressed as $\varepsilon_h + \upsilon_s \varepsilon_\ell$, where ε_h = hoop strain, υ_s = Poisson's ratio for steel, and ε_ℓ = longitudinal strain, with the magnitude of displacement ductility factor just above the block $|\mu_T|$ and beneath the block $|\mu_B|$ is shown in Figure 12 for sections of unit 3. The behaviour shown is also typical of units 1, 2 and 4. At the extreme longitudinal compression fibres of the strain gauged sections, the uniaxial yield strain was exceeded in the circumferential direction on first loading to a displacement ductility factor of $\mu = 3$, and the uniaxial strain-hardening strain was exceeded at $\mu = 7$. The strain rosettes on the diameter perpendicular to the direction of load application indicated lower hoop tensions, with a maximum value of approximately half the uniaxial yield strain being attained during static testing.

Strain rosettes for units 5 and 6 indicated negligible confining strains, $\varepsilon_h + \upsilon_s \varepsilon_\ell$, and shear strains $\gamma_{h\ell}$; as could be expected with the concentrated plastic damage occurring 150 mm away at the position within the block where the casing was curtailed.

Tensile Strains in the Spiral Reinforcement

The tensile strains in the spiral reinforcement at the sections 100 mm from the central stub are plotted against $|\mu_T|$ or $|\mu_B|$ for unit 3, which was similar to that of unit 4, in Figure 13. Gauges b and d, representing the confining influence of the spiral reinforcement on the concrete as they are in the vicinity of the peak longitudinal compression strains, show yielding at $\mu \geq 4$. However, gauges at a and c, which represent the effectiveness of the spiral reinforcement in carrying shear, are comparatively lightly strained as they indicate that yield was not reached. The strain gauges, in the same position, on specimens 5 and 6 showed lower strains than those for specimens 3 and 4 which was consistent with the data from the strain rosettes.

Check of the Bernoulli-Navier Hypothesis

Figure 14 indicates the typical longitudinal strains attained for given levels of μ at the section which was 100 mm beneath the block in unit 3; the results were similar for unit 4. For $\mu \leq 2$ strains were close to being linearly proportioned across the section which implied that the Bernoulli-Navier hypothesis of plane sections remaining plane on bending was valid. For levels of $\mu > 2$ wide scatter of strains is obvious; probably due to concrete cracking, shear deformation, and local buckling, which indicated violation of the hypothesis. However the figure does indicate that composite action was effective at the section as at the higher ductility levels most of the casing perimeter and most of the reinforcing bars were yielding. It is also significant to note that part of the casing was strain-hardening at $\mu = 6$.

Curvature Profiles

Curvature profiles for unit 3 are illustrated in Figure 15. Dial gauges measured average curvatures over 300 mm gauge lengths adjacent to the central loading block compared with the bulging region which had a length of 60 mm. It is thus probable that peak curvatures reached after buckling commenced at $\mu = 4$ were substantially higher than those indicated. The theoretical yield curvature, ϕ_y defined similarly to Δ_y, was exceeded over 38% of the total height of the unit. It is also evident that between cycles at each ductility level the curvature was being redistributed from zones of low curvature into zones of higher curvature as a result of minor load degradation between successive peaks at the given ductility level. This phenomenon was more noticeable at high ductility levels as the plastic damage increased.

Longitudinal Strains in the Casing for Units 5 and 6

Longitudinal strain profiles, at the extreme fibres of the casing under bending for the portion of unit 6 beneath the block are shown in Figure 16. The strain patterns for unit 5 were similar but of lower magnitude. The extreme fibre strains are shown for the peaks of the first cycle to $\mu = 3/4$, 2, 4, 6, 8, 10, 14 and 18. Figure 16 indicates a trend towards longitudinal compression strains in excess of yield for $\mu > 2$ and longitudinal tension strains of negligible value at the section 50 mm into the block where the casing is curtailed. The high compression strains would be due to the casing bearing into the highly confined concrete inside the block, whilst the negligible tension strains would be due to the lack of anchorage for the casing at that section. Bond conditions in this unit appear to be good enough for composite action to develop along much of the length of the specimen. It is also obvious that bond

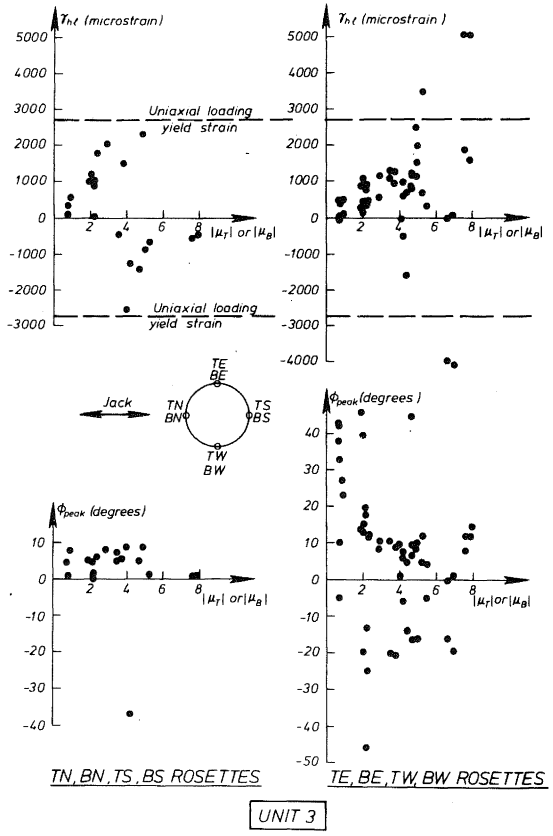

Fig. 11 - Shear Strains in the Casing

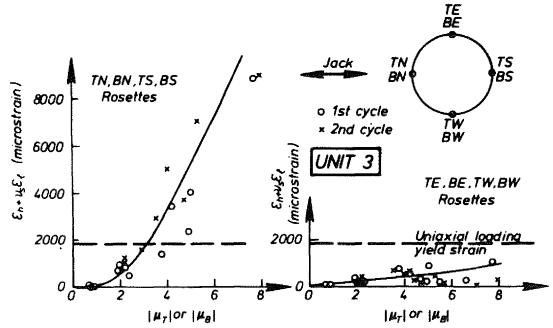

Fig. 12 - Confining Strains in the Casing

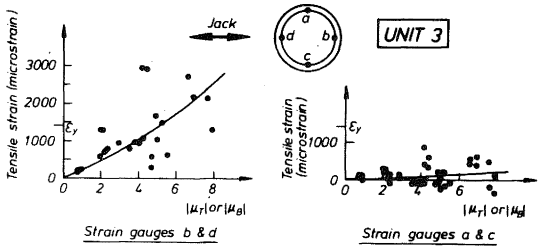

Fig. 13 - Tensile Strains in the Spiral Reinforcement

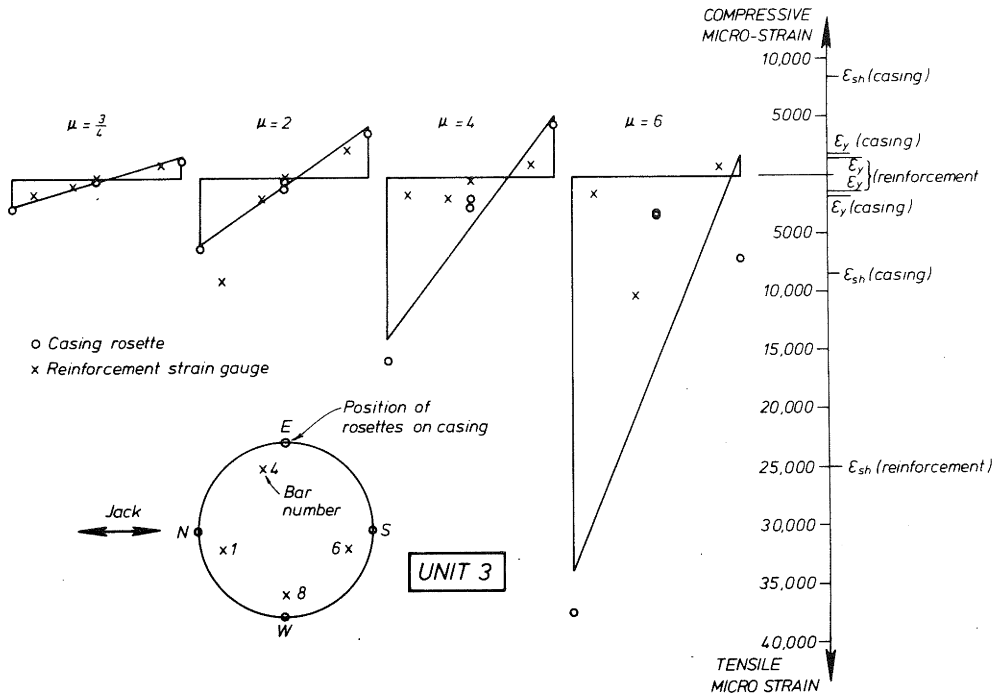

Fig. 14 - Check of the Bernoulli - Navier Hypothesis

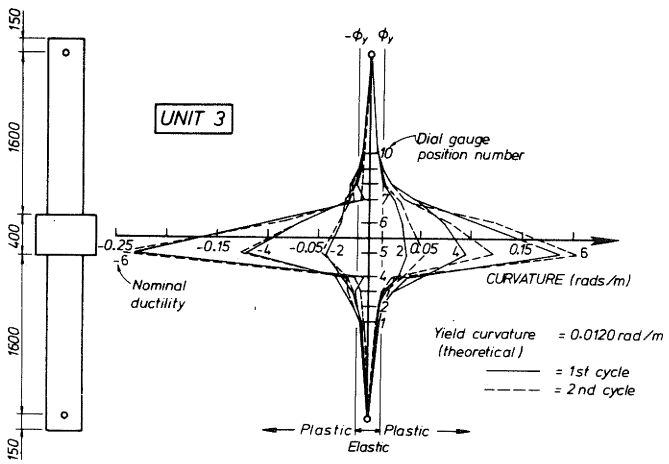

Fig. 15 - Curvature Profiles

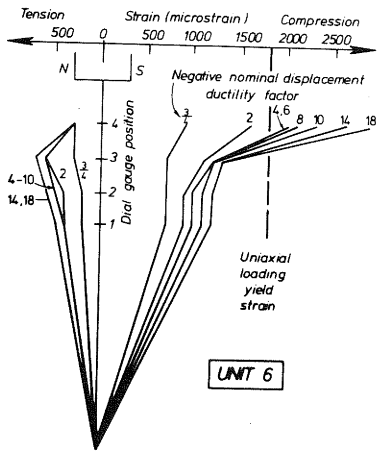

Fig. 16 - Longitudinal Strains in the Casing

conditions appear to improve with increasing μ. This would probably be due to the fact that at high compression strains the concrete has a higher Poisson's ratio than the steel; and thus high friction forces would result as the concrete tries to expand outwards against the casing.

ANALYSIS OF RESULTS:

Ultimate Flexural Capacity

Table 2 contains five different methods, all corrected for P-Δ effects, for predicting the flexural capacity of the test units based on their measured properties. The moment from the moment-curvature analysis (column 5) with an extreme concrete compression fibre strain of 0.003 was, as expected, in close agreement with the equivalent A.C.I. capacity (column 4). The maximum discrepancy between the two methods was 3%. The upper bound response (column 7) assumed that the casing was behaving to its uniaxial loading capacity in both the hoop and longitudinal directions, while the lower bound response (column 8) assumed the casing was behaving uniaxially in the longitudinal direction only. The "confined" moment (column 9) assumed the casing was only acting to confine the concrete. The upper bound, lower bound and confined moments listed in the table were the maximum moments obtained from the moment-curvature analyses up to the maximum deformations sustained by the test units.

The theoretical upper and lower bound responses for units 1 to 4, which both assumed full composite action, closely bracketed the maximum experimental moment. Units 5 and 6 however were 39% and 29% respectively stronger than the "confined" prediction. The percentage over-strength available above the equivalent A.C.I. moment is also shown in table 2. Units 1 to 4 showed moderate strength gains. For units 1 and 3, $P/f'_cAg = 0.1$, the overstrength was about 18%, and for units 2 and 4, $P/f'_cAg = 0.3$, the overstrength was 26%. Units 5 and 6 showed overstrength of 87% and 69% respectively indicating the influence of the casing which had been ignored in the equivalent A.C.I. capacity. The increase in flexural strength with increasing axial load is also very much in evidence by comparing the test units within each pair.

Table 2 also compares the experimentally and analytically obtained yield deflections Δ_y. Excellent agreement was obtained for units 1 to 4 with an average difference of only 3%. Thus the assumption that the pile curvature, illustrated in Figure 8, within the central stub was identical to that at the face of the stub was reasonable. The initial theoretical estimates of the deflection for units 5 and 6, which ignored any casing stiffness were found to be approximately three times as large as the experimental values. However, revised estimates indicated byparentheses, which assumed the load-deflection characteristics of units 5 and 6 were identical to those for units 3 and 4 respectively, up to the value of H_{ACI} for units 5 and 6, gave close estimates of the deflections for units 5 and 6.

Shear Carrying Mechanisms

Table 3 compares the estimated shear forces carried by the casing, spiral reinforcement and the concrete at sections 200 mm from the block for test units 1 to 4. Shear carried by the concrete has been calculated by subtracting the casing and spiral reinforcement contributions from the total shear measured at ductility factors of $\mu = 2$, 4 and 6. The shear force carried by the casing was estimated by assuming that the shear stress in the casing τ, t the diameter perpendicular to the loading axis in the casing was defined as in equation 5,

$$\tau = \frac{\gamma_{h\ell} E_s}{2(1 + \upsilon_s)} \qquad (5)$$

where E_s = Young's Modulus in the steel. This equation probably over- estimates the casing stress at post-elastic levels. The shear force carried by the casing V_{casing} was then calculated by using equation (6).

$$V_{casing} = \frac{2\tau It}{Q} \qquad (6)$$

where I = second moment of area of the casing, t = casing thickness, Q = first moment of area of the casing above the diameter perpendicular to the loading axis. Shear carried by the spiral reinforcement was calculated using measured steel stresses and assuming a 45° diagonal tension crack. On this basis the shear carried by the spiral reinforcement V_{spiral} was calculated from equation (7).

$$V_{spiral} = \frac{4D_s . A_{sp} . f_s}{\pi . s} \qquad (7)$$

where D_s = diameter across the spiral reinforcement centres, A_{sp} = area of spiral reinforcing bar, s = pitch of spiral reinforcement, f_s = spiral reinforcement stress.

It should be noted that the wide scatter in $\gamma_{h\ell}$ and the fact that τ could be overestimated implies that the results are of qualitative rather than quantitative value; with the likely shear force carried by the concrete being underestimated.

Nevertheless, it can be seen for units 1 to 4 that the shear carried by the concrete decreased with increasing ductility factor; that units with $P/f'_cAg = 0.3$ have more shear force carried by the concrete than those with $P/f'_cAg = 0.1$; and that test units 3 and 4 which had internal reinforcing cages appear to carry more shear force in the concrete than units 1 and 2 respectively. The average shear stresses in the concrete

Specimen	(1) $\frac{P}{f'_c A_g}$	Δy (mm)		MOMENT (kNm)						(10) Over-strength available from A.C.I.	Σ|μ|		Max(13) $\|\mu_T\|$ or $\|\mu_B\|$
		(2) Experiment	(3) Theory	(4) Equivalent A.C.I.	(5) Moment Curvature at $\varepsilon_c = 0.003$	(6) Maximum experi-mental	(7) Upper bound	(8) Lower bound	(9) Conf-ined		(11) Static	(12) Dynamic	
1	0.1	14.4	14.4	285	283	335	341	313	-	18	51	56	8.3
2	0.3	12.6	13.9	299	304	376	383	-	-	26	67	43	7.8
3	0.1	14.5	14.3	334	341	397	406	392	-	19	53	131	7.9
4	0.3	14.3	14.3	344	355	435	460	432	-	26	81	-	12.4
5	0.1	3.2	9.7(3.3)	100	103	187	-	-	135	87	303	-	67.1
6	0.3	3.2	8.5(3.9)	128	132	216	-	-	168	69	326	1620	104.4

TABLE 2 - Summary of Test Results

v_c, according to the requirements of NZS 3101 (5) for plastic hinge areas and the experimental value are also indicated in table 3. It is clear that the two values are in poor agreement.

Ductility Criteria

Current seismic design philosophy (9) for ductile bridge systems implies that satisfactory hysteretic behaviour, without significant strength degradation, should occur at displacement ductility factors of 6. Slightly less stringent requirements are included in the New Zealand Loadings Code for Buildings NZS 4203 (10) which requires 4 complete cycles to $\mu = \pm 4$ with strength degradation not greater than 20%. This latter provision corresponds to a cumulative displacement ductility factor of $\Sigma|\mu| = 32$. All of the test units as shown in table 2 and by the hysteresis loops of Figure 10 exhibited satisfactory performance when judged by the criteria of adequate strength at $\mu = 6$ and $\Sigma|\mu| = 32$. In the case of units 5 and 6 these criteria were exceeded by a factor of at least 9. However, the pinched nature of the hysteresis loops might imply that the prototype piles would be subjected to higher ductility levels than those predicted on the basis of elasto-plastic response.

Table 4 indicates the estimated maximum concrete compression strain ε_c, and curvature ductility demands sustained by units 1 to 4 during static testing. The gauge length of 300 mm was clearly too large to measure the peak values and thus the peak values estimated to exist at the bulges are also given. The available ductility of the specimens which were still sustaining in excess of their theoretical A.C.I. strength at ε_c values of approximately 20% is clear; as are the extremely high curvature ductility factors, which were of the order of 100, created by the local buckling.

CONCLUSION:

The model steel encased concrete piles exhibited satisfactory seismic performance with predictable strength, and ductility capacity exceeding current requirements for bridges and buildings in New Zealand. However, it was evident that local buckling of the casing, for units with continuous casing at the central section, occurring at $\mu = 4$ somewhat limited the potential for ductile performance in the test units. Thus it is possible that prototype piles with values of casing diameter to thickness greater than 72, that used in the experimental series, could perform less favourably under seismic loading because of a greater propensity towards local buckling.

The significance of the casing to the structural performance was clearly marked. For units 1 to 4, the models with continuous casing, at a design level ductility factor of $\mu = 6$ the casing was contributing approximately 70% of the flexural strength and 95% of the shear strength. The resulting overstrengths, from the theoretical ultimate based on 0.003 concrete strain, strain compatibility and measured material properties, at peak deformation were of the order of 20%. For units 5 and 6, which did not possess well-anchored casing at the critical flexural section, a vast capacity for load carrying at large displacements existed. The casing, due to its concrete confining role and the end bearing developed at the critical sections, enabled overstrengths of approximately 80% to develop from the theoretical ultimate, which was calculated as for units 1 to 4 but ignoring the casing.

Finally, it was found that the requirements of NZS 3101 with regard to a minimum steel encasement thickness, as expressed in equation (1), are conservative for concrete filled steel tubes.

ACKNOWLEDGEMENTS:

Financial assistance from New Zealand Railways and the University of Canterbury is gratefully acknowledged. This research was part of a Master of Engineering project by Park, supervised by Priestley and Walpole.

BIBLIOGRAPHY:

1. Knowles, R.B., "Steel Tube Columns Infilled with Concrete", Master of Engineering Thesis, University of Canterbury, Christchurch, New Zealand, 1967.

2. Neoghi, P.K., Sen, H.K., and Chapman, J.C., "Concrete-filled Tubular Steel Column Under Earthquake Loading", The Structural Engineer, Vol. 47, No. 5, May 1969.

3. Ang Beng Ghee, "Ductility of Reinforced Concrete Bridge Piers Under Seismic Loading", Master of Engineering Report, University of Canterbury, Christchurch, New Zealand, 1981.

4. Blakeley, R.W.G., "Ductility of Prestressed Concrete Frames Under Seismic Loading", Doctor of Philosophy Thesis, University of Canterbury, Christchurch, New Zealand, 1971.

5. "Code of Practice for the Design of Concrete Structures", NZS 3101, Standards Association of New Zealand, Wellington, 1982.

6. Park, R.J.T., Priestley, M.J.N., Walpole, W.R., "The Seismic Performance of Steel Encased Reinforced Concrete Bridge Piles", Research Report 82-12, Civil Engineering Department, University of Canterbury, Christchurch, New Zealand.

7. Leslie, P.D., "Ductility of Reinforced Concrete Bridge Piers", Master of Engineering Report, University of Canterbury, Christchurch, New Zealand 1974.

8. Mander, J.B., "Ductility of Reinforced Concrete Hollow Bridge Piers", Doctor of Philosophy Thesis in Preparation, University of Canterbury, Christchurch, New Zealand.

9. Berrill, J.B., Priestley, M.J.N., and Chapman, H.E., "Design Earthquake Loading and Ductility Demand", Bulletin of the New Zealand National Society for Earthquake Engineering, Vol. 13, No. 3, September, 1980.

10. "Code of Practice for General Structural Design and Design Loadings for Buildings", NZS 4203:1976, Standards Association of New Zealand, Wellington, New Zealand.

I.J. Garrett:

Reinforced masonry experience indicates a shrinkage gap between core and shell. Did this gap appear at all in the experiments described?

The Authors:

No shrinkage gap was observed and response tended to follow the moment-curvature analyses which assumed composite action was achieved. Thus shrinkage effects were probably unimportant.

M. Wakabayashi (Disaster Prevention Research Institute, Kyoto University, Kyoto, Japan):

In this type of column you can select arbitrally the combination of reinforcing bar amount and tube thickness. When the tube is too thin local buckling might occur and also shear failure might occur. In what way do you select the proportions of tube and reinforcing bars?

TABLE 1 - Actual Test Unit Details

Specimen	f'_c	$\frac{P_e}{f'_c A_g}$	Longitudinal bars		5 mm Casing		Spiral Steel in Plastic Hinge Region	
			No. of D16 bars	f_y	Continuous	f_y	R10 Spacing	f_y
1	28	0.1	-	-	Yes	370	-	-
2	28	0.3	-	-	Yes	370	-	-
3	28	0.1	9	315	Yes	370	70	295
4	28	0.3	9	315	Yes	370	35	295
5	29	0.1	9	315	No 50 mm cap embedment	370	70	295
6	29	0.3	9	315	No 50 mm cap embedment	370	35	295
Units	MPa	-	-	MPa	-	MPa	mm	MPa

DISCUSSION:

I.J. Garrett (Ministry of Works and Development, Wellington):

Not only rusting but abrasion could result in a significant loss of cylinder strength. Any comment?

The Authors:

Yes, this could be a problem. The MWD Culvert Manual provides for a loss of 0.10 mm/year to allow for rusting and abrasion on steel.

The Authors:

It has been customary to select a 10 mm casing thickness for satisfactory construction performance and then to provide reinforcement to achieve any increase in flexural strength desired. The tubes have a large amount of shear strength and thus shear failure is ruled out. Local buckling is a problem with thin tubes. However further tests have shown that casing diameter to thickness ratio (D/t) of up to 150 will still result in satisfactory performance.

TABLE 3 - Shear Distribution

Unit	μ	P/f'_cA_g	(micro-strains) $\gamma_{h\ell}$	(kN) V_{casing}	(micro-strains) ε_{spiral}	(kN) V_{spiral}	(kN) V_{total}	(kN) $V_{concrete}$	v_c (MPa)	
									Expmnt.	Code
1	2	.1	500	110	-	-	195	85	0.88	0
	4	.1	1000	> 209	-	-	209	0	0.00	0
	6	.1	2500	> 209	-	-	209	0	0.00	0
2	2	.3	500	110	-	-	218	108	1.12	1.89
	4	.3	800	176	-	-	228	52	0.54	1.89
	6	.3	1000	220	-	-	222	2	0.02	1.89
3	2	.1	400	88	50	4	228	136	1.41	0
	4	.1	1000	270	100	8	245	17	0.18	0
	6	.1	2000	> 245	150	16	245	0	0.00	0
4	2	.3	400	88	50	8	239	143	1.49	1.89
	4	.3	500	110	100	16	250	124	1.29	1.89
	6	.3	1000	220	150	32	256	4	0.04	1.89

TABLE 4 - Maximum Deformations

Unit	Curvature Ductility Demand		ε_c (%)		Maximum of $\lvert\mu_T\rvert$ or $\lvert\mu_B\rvert$
	300 mm gauge length	concentrated at 60 mm long bulge	300 mm gauge length	concentrated at 60 mm long bulge	
1	20.2	101	4.2	21	8.3
2	15.6	78	4.7	24	7.8
3	20.5	103	4.7	24	7.9
4	22.2	111	3.6	18	12.4

Gideon Kusuma (Indonesia):

Asked what mechanism retained the hysteretic loop after local buckling; was it due to the post buckling or concrete restraint?

The Authors:

Both mechanisms maintain the satisfactory hysteretic performance of the piles after buckling. Hoop tensions in the casing ensures that the bulges do not grow outwards and the internal concrete core prevents the casing from failing in a dimpled fashion as an empty steel cylinder does under crushing load.